Int. J. Heat Mass Transfer. Vol. 31, No. 10, pp. 2091–2100, 1988
Printed in Great Britain

0017–9310/88 $3.00+0.00

Convective film boiling in a rod bundle: axial variation of nonequilibrium evaporation rates

C. UNAL,† K. TUZLA, J. C. CHEN, S. NETI and O. BADR‡
Institute of Thermo-Fluids Engineering and Science, Lehigh University, Bethlehem, PA 18015, U.S.A.

(*Received* 21 *July* 1987 *and in final form* 10 *March* 1988)

Abstract—An experimental study of convective film boiling (post-CHF) is carried out for two-phase steam–water flow in a nine-rod bundle test section. Measurements of wall heat flux, wall superheat, and vapor superheat are obtained as a function of axial distance from the critical heat flux (quench front) for a range of flow rates and flow qualities. These data permit the evaluation of the effective evaporation ratio (fraction of total heat input causing net vapor generation) as a function of test conditions and axial distance from the quench front. The results indicate the existence of a 'near region' with significant evaporation, followed by a far region where the effective evaporation ratio decreases to less than 10% of the total heat input. While the wall and vapor superheats measured in these rod bundle experiments differ in magnitude from those obtained in earlier single tube experiments, qualitative agreement in the axial behavior of the post-CHF process is observed. These data are presented in the hope of aiding attempts to develop improved mechanistic models for convective film boiling heat transfer.

INTRODUCTION

CONVECTIVE boiling after exceeding the critical heat flux can be encountered in steam generators, refrigeration systems, cryogenic systems, nuclear reactors and other applications. This regime of boiling is sometimes referred to as 'convective film boiling', 'post-CHF heat transfer', 'post-dryout boiling', or 'flow-film boiling'. The flow pattern is either inverted annular flow (liquid core surrounded by a vapor annulus) or fully dispersed flow (liquid drops dispersed in a vapor continuum). In either case, superheating of the vapor above the saturation temperature can occur, resulting in thermodynamic nonequilibrium between the two phases [1–7]. This state is characterized by a superheated vapor and an actual flow quality (X_a) less than the thermodynamic equilibrium quality (X_e). Energy balance requires that

$$X_e h_{fg} = X_a[h_{fg} + C_{pv}(T_v - T_s)] \tag{1}$$

and if

$$T_v > T_s$$

then

$$X_a < X_e. \tag{2}$$

Analysis of convective film boiling requires knowledge of the degree of vapor superheating and the resultant degree of thermodynamic nonequilibrium. Of particular importance is the axial variation of vapor superheat (in the direction of flow) since the intensity of vaporization (Γ) is characterized by the axial derivative of the vapor temperature

$$\Gamma = \frac{(\text{Mass of liquid vaporized})}{(\text{Time}) \cdot (\text{Volume})}$$

$$= G\frac{dX_a}{dz}$$

$$= G\frac{d}{dz}\left[\frac{X_e h_{fg}}{h_{fg} + C_{pv}(T_v - T_s)}\right]. \tag{3}$$

Finally, since only a fraction of the heat transfer to the fluid effects vaporization of the liquid phase (the balance going toward superheating of the vapor), one is concerned with the 'evaporation ratio', defined as

$$R_E \equiv \left(\frac{\text{Latent heat of vaporization}}{\text{Time} \cdot \text{Volume}}\right) \div \left(\frac{\text{Total heat input}}{\text{Time} \cdot \text{Volume}}\right)$$

$$= \frac{h_{fg} \cdot \Gamma}{Q/V}. \tag{4}$$

Due to the difficulty of measuring vapor superheat in the presence of dispersed liquid, only a few attempts to quantify the degree of thermodynamic nonequilibrium have been reported. Mueller [8], Polomik [9], Nijhawan *et al.* [10], Annunziato *et al.* [11], Gottula *et al.* [12] and Evans *et al.* [13] were successful in obtaining measurements of nonequilibrium vapor superheats for post-CHF boiling in vertical tubes. Of these, only the latter two studies [12, 13] obtained

† Present address: Department of Chemical and Nuclear Engineering, University of Maryland, College Park, MD 20742, U.S.A.

‡ Present address: UAE University, Alain, P.O. Box 15551, United Arab Emirates.

NOMENCLATURE

C_p	specific heat [kJ kg^{-1}°C^{-1}]
h_{fg}	specific latent heat of vaporization [kJ kg^{-1}]
G	mass flux [kg m^{-2} s^{-1}]
p	pressure [kPa]
Q	heat [kJ]
R_E	evaporation ratio [—]
T	temperature [°C]
X	vapor mass quality [kg kg^{-1}]
V	volume [m^3]
z	axial distance [m].

Greek symbol

Γ	vapor generation rate [kg m^{-3} s^{-1}].

Subscripts

a	actual
CHF	critical heat flux
e	equilibrium
in	inlet
r	rod
s	saturation
v	vapor
w	wall.

information on the axial variation of the vapor superheats. There is also concern that the thermodynamic behavior may be affected by channel geometry; and since many applications involve flow in rod or tube bundle geometries, there is a need to characterize the nonequilibrium behavior in bundles.

The objective of the present study was to obtain experimental measurements of post-CHF boiling in a rod bundle geometry, including information on the axial variation of vapor superheats. The aspirated probe technique of Nijhawan *et al.* [10] was modified to permit measurements of vapor superheats in the flow channels of the rod bundle. To obtain axial variation information, the procedure of Evans *et al.* [13], utilizing slowly propagating CHF quench fronts was adopted.

EXPERIMENTAL

The experiments were carried out in a two-phase loop with a vertical rod bundle test section. The loop provided a metered flow of known flow rate, pressure, and vapor/liquid quality to the inlet of the test section. The test section consisted of a heated shroud containing a 3 × 3 rod bundle assembly, as illustrated in Fig. 1. Dimensions of the rods and the shroud were selected so as to have equal hydraulic diameters in all flow subchannels (e.g. cells I and II). Figure 2 shows a schematic diagram of the test section and its inlet and exit connections. The inlet section provided a flow length with an internal strainer to obtain good mixing between the vapor and liquid phases. A hot patch was also available to condition the thermal state of the inlet two-phase flow and to stabilize the quench front for those tests where a fixed CHF point was desired. Stainless steel was used as the material for the test section walls that are exposed to the fluid (i.e. Inconel 625 for shroud, and SS-316 for rod cladding). After the initial change in color, no scorching or additional discoloration were observed. The test section had a length of 1.2 m and incorporated four ports for vapor temperature and pressure probes and a rod spacer, as

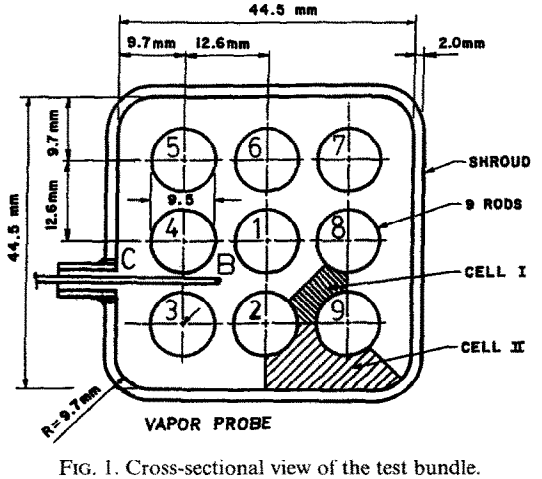

FIG. 1. Cross-sectional view of the test bundle.

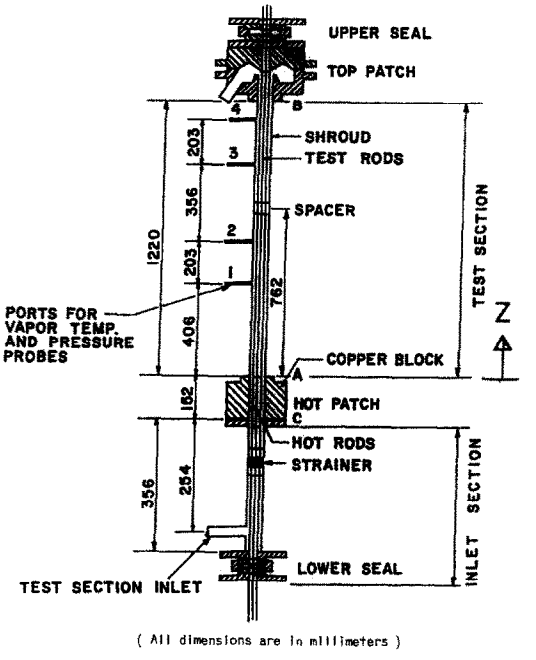

FIG. 2. Schematic diagram of the test section.

indicated in Fig. 2. The vapor superheat probes were similar to those used by Nijhawan *et al.* [10] and Evans *et al.* [13], modified to permit traversing across the rod bundle width (from point B to C in Fig. 1). Reported vapor temperatures here, however, were measured while the probe tip was located at the centerline of the inner cell (point B in Fig. 1). The nine test rods were electrically heated through internal coils fed by d.c. power, with uniform heat flux. The test section shroud was heated by a radiant furnace with multi-zone control. Thermocouples mounted on the external wall of the shroud permitted determination of shroud temperatures along its axial length. Each of the nine internal rods were equipped with 12 thermocouples embedded in grooves near the rod surface for measurement of wall temperatures at various axial and angular locations. Due to a limited channel capacity (90 channels) of the data acquisition system, however, only 80 thermocouples were recorded during an experimental run. In addition to the rod and shroud's power and temperature measurements, the fluid flow rate, inlet enthalpy, inlet pressure, and core vapor superheats were determined and recorded for each run. Standard grade chromel–alumel thermocouples were used for all temperature measurements. The thermocouple which measured the saturation temperature was calibrated by a reference thermometer with an estimated uncertainty of ± 0.4°C. The wall thermocouples were then calibrated with reference to the above thermocouple. Total uncertainty on wall temperature measurements was ± 2°C as estimated in ref. [18]. Vapor temperature measurements included additional uncertainties due to chart reading, and the uncertainty was ± 5°C [18]. Electrical power inputs to the various parts of the loop were measured with power transducers, with an accuracy of $\pm 1\%$ of full scale. The flow rate was measured under single phase conditions with an accuracy of 0.5% of full scale. The final uncertainty on equilibrium quality in the test section, therefore, was a dependent to operating conditions and ranges of power meters and flow meters. Detailed analysis is provided in ref. [15]. It is concluded that, at worse, the uncertainty on the equilibrium quality at the test section inlet would be less than 1%, and at the test section outlet it would be less than 2%. Details of the test facility and instrumentation are also given in ref. [15].

In a typical experimental run, the test section would be preheated to a selected post-CHF state with the shroud and rods at substantial superheats. A steady two-phase flow, with desired flow rate, pressure, and inlet mixture enthalpy would be established, using a bypass around the test section during the preheating stage. For the runs with propagating quench front (moving CHF location) the inlet hot patch was maintained as an adiabatic section at the fluid saturation temperature. Upon obtaining the desired initial condition, data acquisition was started and the two-phase fluid would be switched from the bypass line to the test section. Ninety channels of experimental data would be recorded on a 7 s time cycle through the duration of each test run.

As the two-phase fluid passed through the test section, post-CHF boiling occurred along the length of the test section downstream of the CHF point. By adjustment of the power input to the test rods and shroud, it was possible to attain a steady upward movement of the CHF location (propagating quench front) as the test section slowly cooled. Because the quench front velocity was orders of magnitude less than the fluid flow velocity, sufficient time was obtained to establish thermal-hydraulic quasi-steady state downstream from the quench front through the course of each run. In this manner, measurements of vapor superheats at the probe location could be analyzed to obtain axial variations of the degree of nonequilibrium as a function of distance from the CHF point. In a typical run, the quench front would propagate with a velocity of the order of 1 mm s^{-1}, and a single run would last approximately 10 min (time for the quench front to reach the vapor probe station).

All experiments were carried out with water/steam as the test fluid. A total of 50 experiments were completed, generating 276 sets of data. The two-phase mass flux ranged from 7 to 26 kg m^{-2} s^{-1}, and the inlet mixture enthalpy varied from 40°C subcooled to 50% net quality (equilibrium quality). The test pressure was slightly above the atmospheric pressure.

RESULTS

The primary information recorded was the time-varying temperatures of the heater rods and two-phase vapor. Figure 3 shows a representative plot of the transient rod surface temperatures as a function of time, at three different axial locations in the test section. Starting with a uniform initial superheat (approximately 560°C for this run), local zones of the rod underwent different thermal-hydraulic histories before being quenched by the two-phase flow. The region nearest the entry showed immediate cooling upon introduction of the two-phase fluid, having a period of approximately 100 s in post-CHF heat transfer before being quenched to the saturation temperature. At higher elevations, the rod surface experienced a mild increase in temperature before prequench cooling by the two-phase flow. For the purposes of this study, the time of local quench at each thermocouple location was defined as the moment of maximum cooling rate (as measured from the time derivative of the wall temperatures). As indicated by the dark symbols in Fig. 3, this quench point consistently occurred at a surface superheat of approximately 200°C.

Figure 4 shows a plot of the rod and vapor temperatures measured along the length of the test section, at a particular time (70 s) after initiation of two-phase flow. The open circles represent surface

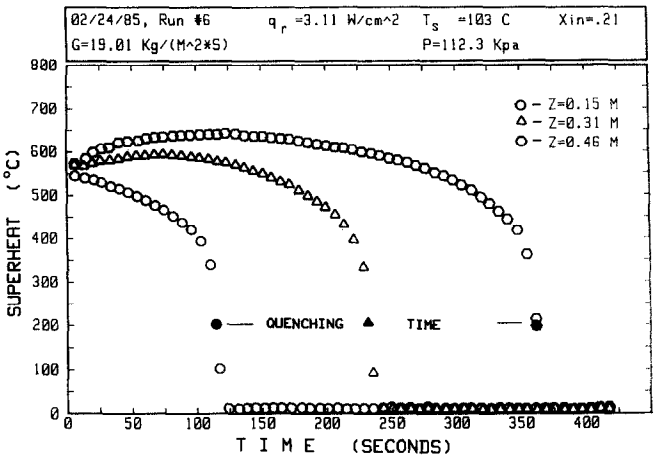

FIG. 3. Wall superheat vs time at three axial locations for the center rod.

temperatures measured on the nine rods in the test section at the various elevations indicated. The uniformity and smoothness of this composite curve confirms the similarities of thermal-hydraulic conditions in all flow subchannels of the rod bundle. The axial variation of the rod temperatures shown in Fig. 4 is typical for all tests. Upstream of CHF (quench front), the rods' surface superheats were essentially zero; immediately downstream of the quench front, the rods experienced a rapid rise in temperature to several hundred degrees centigrade in a distance of approximately 0.3 m. Further downstream, the rods were found to have a fairly uniform superheat (of approximately 600°C for this run), with the exception of the region near the grid spacer. At the grid spacer, as indicated by the symbol S in Fig. 4, the rods experienced a sharp decrease in wall superheat, requiring an axial distance of approximately 0.2 m before recovering to the pre-spacer temperatures. This desuperheating effect of the grid spacer was consistently found in all experiments, indicating the promotion of enhanced two-phase cooling by the spacer obstruction. Locations of the vapor probe stations are indicated by the symbol P in Fig. 4. During this experiment, only two of the stations were mounted with vapor probes; the measured vapor temperatures are indicated by the dark symbols in Fig. 4. For the conditions of this test, it is seen that the vapor attains a very significant level of superheat (400°C) just 0.5 m downstream from the CHF (quench front). The downstream measurement did not indicate any significant further increase, due primarily to the desuperheating effects of the grid spacer on the two-phase fluid.

Figure 5 shows 'snapshots' of the rod and vapor superheats as a function of axial position for two times in an experimental run. It is seen that as the run progressed, the CHF quench front propagated upward in the test section. The general characteristics of the downstream wall temperatures remained similar, although there is a discernible decrease in the magnitude of the local wall superheat upon approach of the quench front. The vapor superheats were more significantly affected by the advancing quench front; at the first probe station, the vapor superheat was observed to decrease from 420 to 200°C as the quench front advanced by a distance of approximately 0.25 m in that experiment. The axial variations of rod and vapor superheats shown in Figs. 4 and 5 are illustra-

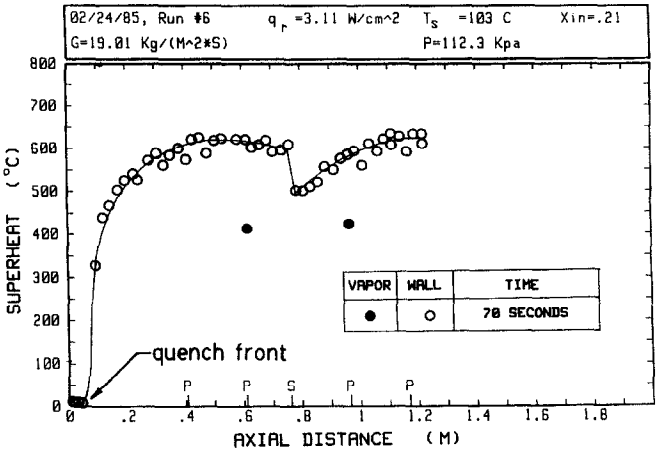

FIG. 4. Typical axial temperature distribution in a moving CHF experiment.

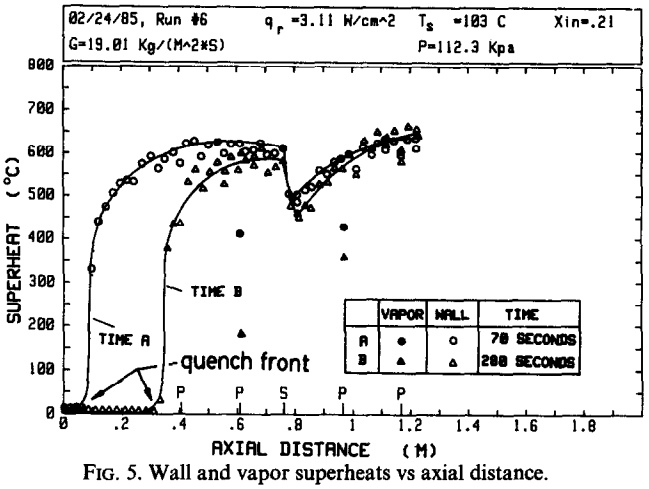

FIG. 5. Wall and vapor superheats vs axial distance.

tive of behavior found in these experiments. Reproducibility was checked by carrying out two or more runs with similar entrance and boundary conditions. It was found that derivations in wall and vapor superheats were of the order of only 3% for similar runs.

The uniformity of thermal-hydraulic conditions for different subchannels in the rod bundle could be assessed by the uniformity of time-to-quench at various elevations for the nine different test rods. Figure 6 plots the quench times for individual thermocouples on the various test rods, as indicated by the numbers corresponding to the layout shown in Fig. 1. It is seen that all nine rods essentially experienced the same quench history. The wall superheat data shown in Fig. 4 also give supporting evidence of thermal-hydraulic uniformity across the rod bundle. It is seen that the rod surface temperatures measured on all the rods at any one moment in the test are clustered about a single axial-variation curve. It was felt that the use of a heated shroud designed to have thermal capacity and heat fluxes similar to those of the internal rods was crucial to obtaining this uniformity across the rod bundle. To our knowledge, this is the first post-CHF experiment to use a heated shroud to alleviate the potential cold-wall effects of a small test bundle. The data plotted in Fig. 6 also indicate the constancy of the quench front velocity in the duration of an experiment. The quench front location was seen to vary essentially linearly with time for all test rods.

During each test run, the total heat transfer to the two-phase fluid was comprised of electrical power input plus the release of stored energy in the heater rods and the shroud. In the data reduction process, transient heat balances were carried out at each scan time to determine the transient heat flux for each rod and for the shroud at various axial locations. Figure 7 shows typical results for a run, 76 s after initiation of two-phase flow, indicating the local heat flux on the center test rod. Upstream of the quench front location, the rod heat flux corresponded to the steady-state electric power input. In the vicinity of the quench front there was a sharp spike in the local heat flux due to the rapid release of stored energy as that section of the rod was quenched from its superheated state. Downstream from the quench front, the heat flux decreased again to the level of the electric power input. Such local heat flux distributions were calculated for all nine test rods and the shroud and summed to

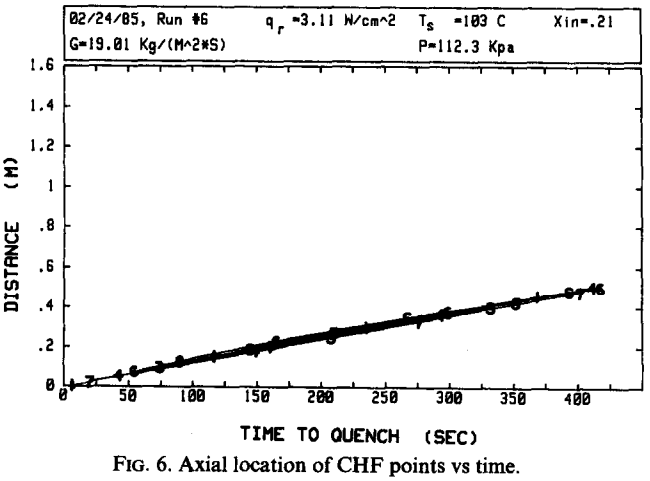

FIG. 6. Axial location of CHF points vs time.

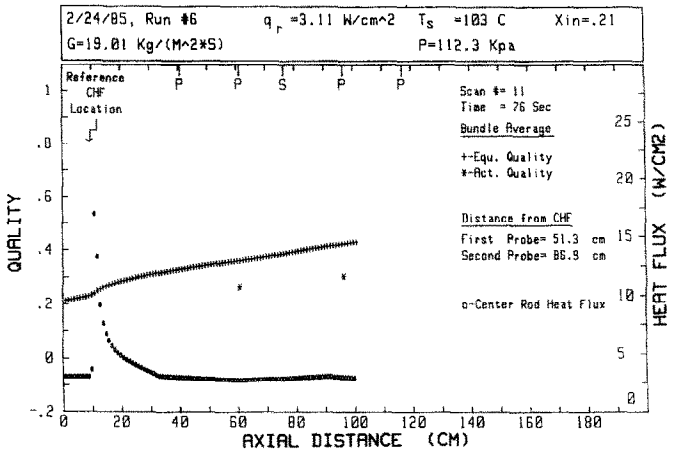

FIG. 7. Typical calculated wall heat fluxes and qualities as a function of distance for a moving CHF data point.

obtain the instantaneous total heat input to the fluid as a function of axial position. This information then permitted calculation of the equilibrium two-phase quality (specific fluid enthalpy) as a function of axial position. For the test conditions illustrated in Fig. 7, it is seen that this equilibrium quality increased from 0.21 at the inlet to 0.45 at the 100 cm position. Over most of the test section, the equilibrium quality increased at a constant rate corresponding to the electric power input. However, in the region near the quench front, a local step increase in fluid enthalpy is obtained due to the spike in local heat flux described above. Also shown in Fig. 7 are the values of the actual flow qualities calculated at the two vapor probe locations. Since the measured vapor temperatures were significantly superheated above the equilibrium saturation temperature, the actual flow quality is seen to be significantly less than the corresponding equilibrium qualities, consistent with equation (1). The conditions indicated in Fig. 7 are representative of the results observed for all the tests, though magnitudes of heat fluxes, flow rates, superheats, and qualities varied with test conditions.

In order to obtain the variation of vapor superheat with axial position, it is necessary to collect experimental measurements for a given set of inlet conditions and downstream boundary conditions. Since the post-CHF regime starts at the CHF (quench front) location it is therefore necessary to use data for equal values of mass flux (G), pressure (p), and equilibrium quality at the CHF point (X_{CHF}). Similarity of downstream boundary conditions require given values of the wall temperature and wall heat flux. These requirements are not easily satisfied in a single experimental run. As illustrated in Fig. 7, the equilibrium quality increases along the test section; thus the quality at the CHF point changes as the quench front propagates along the test section in a test run. To satisfy the requirement for similar initial and boundary conditions, it was necessary to search the complete data base of all runs for subsets having similar boundary conditions and initial inlet conditions at the CHF location. Figure 8 shows a composite plot of the data for such a subset of measurements obtained at similar entrance and boundary conditions. It is seen that both the wall superheat and the vapor superheat data do delineate axial curves for such a composite set of test conditions. Within the range of conditions indicated, these data give a true indication of the variations of the non-equilibrium thermodynamic conditions as a function of axial position from the quench (CHF) point. Figure 9 shows similar composites for two other sets of test conditions, the primary variation being the equilibrium quality at the CHF location (X_{CHF}).

Several important observations can be made from the data shown in Figs. 8 and 9. First, it is seen that the axial variation of vapor superheat consistently shows an S-shaped profile. Thus the derivative of vapor superheat with axial distance (slope of the curves) is small near the CHF point and at far distances from the CHF point, with a higher value at intermediate distances. For a given mass flux of vapor flow, the slope of the axial profile of vapor temperature measures the rate of specific heat addition to the vapor. A steeper slope implies greater heat addition to the vapor and correspondingly a smaller heat contribution to evaporative phase change; conversely, a shallower slope of the vapor temperature profile indicates a larger amount of heat input going to evaporation and thus a tendency for the two-phase fluid to approach thermodynamic equilibrium. The results shown in Figs. 8 and 9 indicate a region of approximately 20–30 cm immediately downstream from the quench front with relatively low values of the vapor superheat and having a fairly shallow slope in the axial variation of vapor superheat. This implies that the vaporization process is relatively efficient in this region near to the quench front location. Evaporation of the liquid phase can be caused by either heat transfer from the superheated vapor to the entrained liquid or from heat transfer from the superheated wall to the liquid. The corresponding driving forces for

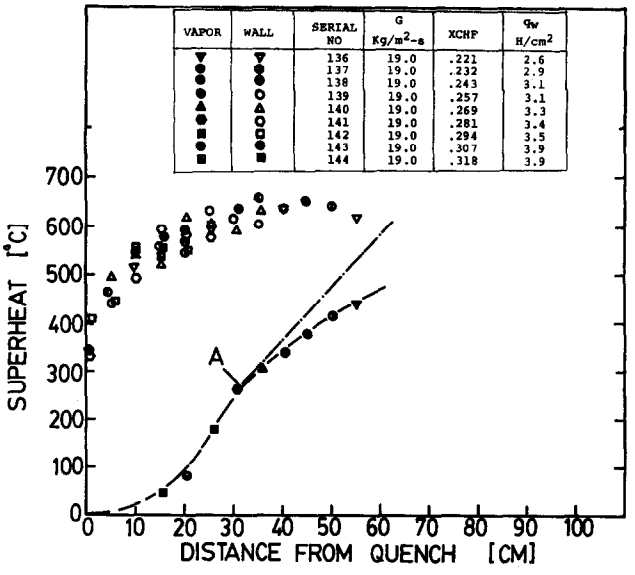

FIG. 8. Vapor superheats and distributions of wall superheat between the CHF point and the first vapor probe for comparable runs.

these two mechanisms are the vapor superheat $(T_v - T_s)$ and the wall superheat $(T_w - T_s)$, respectively. In this near-distance region, the wall superheats are seen to be quite significant while the vapor superheats are relatively low. Thus, the data shown in Figs. 8 and 9 imply that there is an effective mechanism for vaporization in the near region due to direct heat transfer from the wall to the liquid phase. This hypothesis is qualitatively consistent with the observations reported by Hewitt *et al.* [16] and by Ishii [17] which indicate a near-zone region with a relatively large amount of liquid present in a fairly agitated flow pattern which could cause significant liquid splashing on the channel walls.

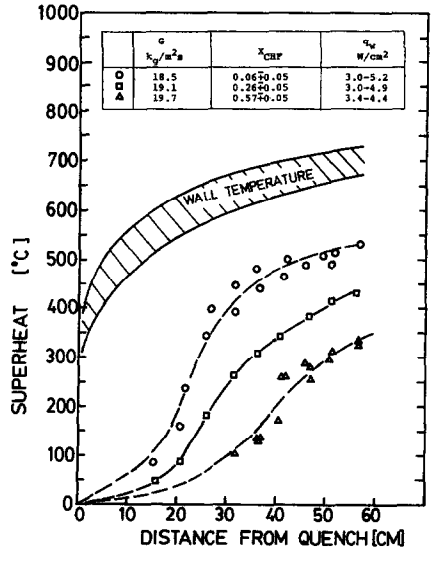

FIG. 9. Wall and vapor superheats vs distance from CHF point for various qualities.

At greater distances downstream from the quench front, the axial gradient of vapor superheat first increases and then decreases with increasing axial distance. It is our belief that the middle region with the high axial gradient indicate that the evaporation process diminishes in intensity due to a reduction of wall-to-liquid heat transfer, as the two-phase flow passes out of the near-region splash zone. This effect continues into the far zone but at these downstream positions the cumulative evaporation has increased the absolute mass flux of vapor flow such that the rate of increase in specific vapor sensible heat (per unit mass of vapor) is decreased even though most of the heat addition still goes toward vapor superheating rather than evaporation. This point can be more easily observed by comparing the axial gradient of vapor superheat to the gradient that would be obtained for the limiting case of 'frozen quality' conditions where all the heat input goes toward vapor superheating. In Fig. 8, a frozen quality line is drawn from point A to indicate the axial profile if no further evaporation were to occur after point A. It is seen that the measured vapor temperature profile lies fairly close to this limiting condition, indicating a relatively ineffective evaporation process in this downstream region.

A final observation can be drawn from the data of Fig. 9, regarding the parametric effect of the two-phase quality. The major variable among the sets of data represented in the figure is the magnitude of the two-phase equilibrium quality at the CHF location (X_{CHF}). The results show that for a given total mass flow rate and a given wall heat flux, there is a significant increase in local vapor superheats as the equilibrium quality decreases. This is consistent with expectations from heat balance that the rate of increase in specific vapor enthalpy would be greater for the case of low vapor flow rates. The data in Fig.

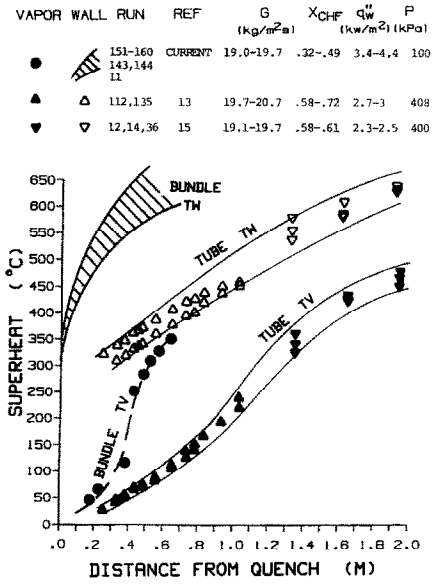

FIG. 10. Wall and vapor superheats vs distance between CHF point and the first vapor probe for the bundle and single tube experiments.

9 also indicate that the extent of the transition region immediately downstream from the quench front increases in length with increasing vapor quality. The implication is that increased vapor flux at the CHF point causes the entrained liquid and the consequent 'splash zone' to extend further downstream from the quench location. Finally, it is seen from Figs. 8 and 9 that the temperature difference between wall and vapor $(T_w - T_v)$ at far distances from the quench front decreases with decreasing quality. Since the vapor convective heat transfer coefficient at the wall would increase with net vapor flow, this observation implies that there is an enhancement mechanism due to the presence of a greater liquid flow fraction which more than compensates for the decrease in pure vapor convection as the quality decreased.

It is of interest to compare these observations for a rod bundle with the published data for post-CHF heat transfer in a single tube, as reported by Evans *et al.* [13] and Gottula *et al.* [12]. Due to the rather limited data base, it was not possible to directly compare data with identical operating conditions. Figure 10 shows a composite plot of results for the rod bundle obtained in this study with data reported for a single tube in refs. [12, 13] at similar values of mass flux and wall heat flux but at different values of pressure and quality at CHF. Due to these differences, no meaningful comparison of absolute wall or vapor superheats can be made. However, it is evident that qualitative agreement in the nature of the axial profiles for both wall and vapor superheats is obtained. Thus the implication of a near region with efficient vaporization, followed by a downstream region of relatively less efficient vaporization, can be made for both in-tube and in-bundle post-CHF heat transfer.

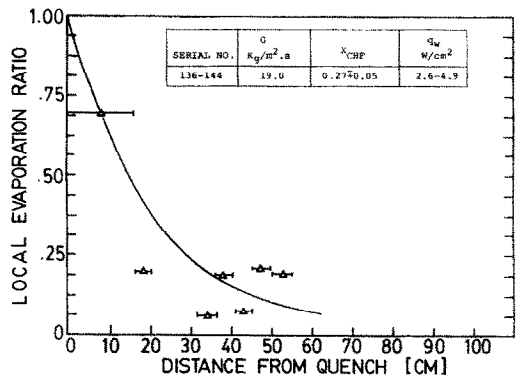

FIG. 11. Evaporation ratio vs distance calculated from comparable runs.

The experimental results of this study permit an evaluation of the net evaporation process as a function of axial distance. Since core vapor superheat is observed in this post-CHF heat transfer process, it is obvious that only a fraction of the total heat input to the two-phase fluid results in vapor formation, the balance being absorbed as sensible superheat of the vapor. To improve our ability for mechanistic modeling of the process one would like to know the division of heat input between evaporation and sensible heating.

The evaporation ratio defined by equation (4), represents the fraction of total heat input that is utilized in vaporization. The evaporation ratio can be expressed locally

$$R_E = h_{fg}\frac{\Gamma}{(Q/V)} = (dX_a/dz)/(dX_e/dz) = \frac{dX_a}{dX_e} \quad (5)$$

or, it can be expressed as an average value between any two axial locations

$$\bar{R}_E = \frac{\int_1^2 dX_a}{\int_1^2 dX_e} = \frac{\Delta X_a|_1^2}{\Delta X_e|_1^2}. \quad (6)$$

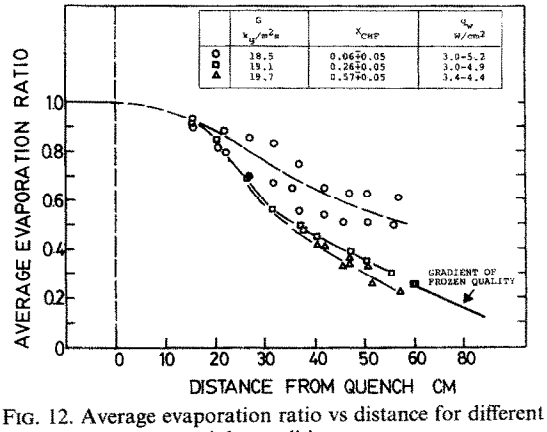

FIG. 12. Average evaporation ratio vs distance for different inlet qualities.

Axial gradients of actual and equilibrium qualities are required for calculation of the local evaporation ratio. A sample case is calculated for the conditions of Fig. 8 and plotted in Fig. 11. The scatter of the data in this figure is partly due to slightly different operating conditions for the various runs that are included, and partly due to experimental accuracy. The data obviously show a decreasing trend in R_E with increasing axial distance. It is seen that the local evaporation ratio approaches unity at CHF (quench front), decreasing to approximately 0.3 at about 20 cm. This decrease continues with increasing axial distance, approaching magnitudes of less than 0.1 after 60 cm. This trend was consistently observed for all tests in this study.

The average evaporation ratio can be calculated from equation (6). Some results are plotted in Fig. 12 for the three experimental conditions reported by the data of Fig. 9. Each point in this figure represents the average evaporation ratio between the test section inlet and the probe location, plotted vs distance between the CHF (quench front) and the probe port. Also shown in the figure is the gradient of the frozen quality conditions at a distance of 60 cm for one of the test conditions. The average evaporation ratios indicate three different regions with increasing distance. Immediately downstream of the dryout quench front (about 10–20 cm), the average evaporation ratio is close to unity and its decrease with distance is rather slow. At distances between 20–40 cm from the dryout quench front R_E decreases faster with increasing distance. In the third region, which is above the 40–50 cm level, the axial gradient of the average evaporation ratio approaches the gradient for frozen quality conditions, indicating that local evaporation is almost zero at these locations.

It is clear that post-CHF heat transfer downstream from the CHF quench front involves a 'near region' with reasonably effective evaporation and a 'far region' where the evaporation process is relatively ineffective and almost all the heat input goes toward sensible superheating of the vapor phase.

The experimental information represented in Figs. 7–11, showing axial variations of heat flux, wall superheats, vapor superheats, and evaporation ratios, are the final results of this study. Clearly, such detailed experimental information is needed to assess and improve models for analysis of the post-CHF heat transfer process. An initial attempt to compare existing models [4, 5, 7] with these data showed unsatisfactory agreement [18]. A few models were reasonably close in prediction of heat fluxes, but essentially all the models did not satisfactorily predict the axial variation of vapor superheating or the evaporation ratio. Clearly, one can have confidence in a phenomenological model only if it can satisfactorily describe the total interacting mechanisms. These experimental findings are presented in this paper in the hope of aiding future developments of improved mechanistic models for the post-CHF heat transfer process. Detailed documentation and tabulation of the data is available in a separate reference report [19].

Acknowledgements—This research was sponsored by the U.S. Nuclear Regulatory Commission under Contract No. NRC-04-81-183. The authors acknowledge with gratitude the continued interest, encouragement, and technical participation provided by Drs Yin-Yun Hsu, Michael Young, Richard Lee and Jose N. Reyes, Program Managers at USNRC, throughout the course of this work.

REFERENCES

1. R. P. Forslund and W. M. Rohsenow, Dispersed flow film boiling, *ASME J. Heat Transfer* **90**, 399–407 (1968).
2. D. C. Groeneveld, The thermal behavior of a heated surface dryout, AECL-4309 (1972).
3. A. W. Bennett, G. F. Hewitt, H. A. Kearsey and R. K. F. Keeys, Heat transfer to steam–water mixtures flowing in uniformly heated tubes in which the critical heat flux has been exceeded, UKAEA Research Group Report AERE-R 5373 (1967).
4. P. Saha, B. S. Shiralkar and G. E. Dix, A post-dryout heat transfer model based on actual vapor generation rate in dispersed droplet regime, ASME Paper No. 77-HT-80 (1977).
5. S. W. Webb, J. C. Chen and R. K. Sundaram, Vapor generation rate in non-equilibrium convective film boiling, *Proc. 7th Int. Heat Transfer Conf.*, Munich, 6–10 September (1982).
6. S. W. Webb and J. C. Chen, A nonequilibrium model for post-CHF heat transfer, *Proc. OECD (NEA) CSNI Third Special Meeting on Heat Transfer and Two-phase Flow*, Pasadena, California, U.S.A., CSNI, Report No. 61, March (1981).
7. S. W. Webb and J. C. Chen, A two-region vapor generation rate model for convective film boiling, *Proc. Int. Workshop on Fundamental Aspects of Post-dryout Heat Transfer*, Salt Lake City, Utah, 1–4 April (1984).
8. R. E. Mueller, Film boiling heat transfer measurement in a tubular test section, EURAEC-1971/GEAP-5423 (1967).
9. E. E. Polomik, Transition boiling heat transfer program—Final Summary Report for Feb/63–Oct/67, GEAP-5563 (1967).
10. S. Nijhawan, J. C. Chen, R. K. Sundaram and E. J. London, Measurements of vapor superheat in post-critical-heat flux boiling, *ASME J. Heat Transfer* **102**, 465–570 (1980).
11. A. M. Annunziato, M. Cumo and G. Palazzi, Post-dryout heat transfer in uncovered core accidents, *Proc. ANS 2nd Nuclear Reactor Thermal-hydraulics Conf.*, Santa Barbara, January (1983).
12. R. C. Gottula, R. A. Nelson, J. C. Chen, S. Neti and R. K. Sundaram, Forced convective nonequilibrium post-CHF heat transfer experiments in a vertical tube, ASME–JSME Thermal Engineering Conf., Honolulu, March (1983).
13. D. Evans, S. W. Webb and J. C. Chen, Axially vapor superheats in convective film boiling, *ASME J. Heat Transfer* **107**, 663–669 (1985).
14. L. E. Hochreiter, NRC/Westinghouse/EPRI FLECHT low flooding rate skew axial profile results, *Proc. 5th Water Reactor Safety Information Meeting*, Washington, DC (1977).
15. K. Tuzla, C. Unal, O. A. Badr, S. Neti and J. C. Chen, Two-phase 3×3 rod bundle test facility for post-CHF boiling, NUREG/CR-3849 (1984).
16. G. F. Hewitt, G. Costigan and D. Lee, UK studies of post dryout heat transfer, *Proc. Twelfth Water Reactor Safety Information Meeting*, Gaithersburg, Maryland, October (1984).

17. M. Ishii, Inverted annular flow experiment at ANL, Private communications, Lehigh University, 21 January (1986).
18. C. Unal, An experimental study of thermal non-equilibrium convective boiling in post-critical-heat-flux region in rod bundles, Ph.D. Thesis, Lehigh University, Bethlehem, Pennsylvania (1986).
19. K. Tuzla, C. Unal, O. Badr, S. Neti and J. C. Chen, *Thermodynamic Nonequilibrium in Post-CHF Boiling in a Rod Bundle*, Vols 1–4, NUREG/CR-5095 (1988).

EBULLITION EN FILM AVEC CONVECTION DANS UNE GRAPPE DE TUBES: VARIATION AXIALE DES FLUX D'EVAPORATION

Résumé—Une étude expérimentale de l'ébullition en film avec convection (post-CHF) est faite sur un écoulement diphasique eau–vapeur d'eau dans une section d'essai d'une grappe de neuf tubes. Des mesures de flux thermique et de surchauffe pariétaux, de surchauffe de la vapeur sont obtenus en fonction de la distance axiale à partir de flux critique (front de trempe) pour des domaines de débit et de qualité d'écoulement. Ces données permettent l'évaluation des taux d'évaporation effective (fraction de la chaleur totale fournie qui cause une production nette de vapeur) en fonction des conditions d'essai et de la distance axiale au front de trempe. Les résultats indiquent l'existence d'une "région proche" avec une évaporation importante, suivie d'une région où le taux d'évaporation effective décroît jusqu'à 10% du flux de chaleur total fourni. Tandis que les surchauffes de paroi et de vapeur mesurées dans ces expériences diffèrent en intensité de celles obtenues dans des expériences précédentes avec un seul tube, un accord qualitatif est observé dans le comportement axial du mécanisme post-CHF. Ces données sont présentées dans l'espoir de favoriser le développement de modèles mécanistes améliorés pour le transfert thermique par ébullition en film avec convection.

FILMSIEDEN BEI ZWANGSKONVEKTION IN EINEM STABBÜNDEL: AXIALE VERÄNDERUNG DER VERDAMPFUNGSRATEN BEI NICHTGLEICHGEWICHT

Zusammenfassung—Das Filmsieden bei Zwangskonvektion einer Dampf–Wasser-Strömung wurde mit einer Meßstrecke bestehend aus einem 9-Stab-Bündel untersucht. In einem weiten Bereich von Massenstromdichte und Dampfgehalt wurden Messungen der Wärmestromdichte sowie der Wand- und Dampfüberhitzung in Abhängigkeit des axialen Abstandes vom Ort der Siedekrise durchgeführt. Die erhaltenen Daten erlauben die Bestimmung des effektiven Verdampfungsanteils (zur Dampferzeugung verbrauchter Anteil an der gesamten zugeführten Wärme) als Funktion der Versuchsbedingungen und des axialen Abstandes vom Ort der Siedekrise. Die Ergebnisse deuten darauf hin, daß eine "nahe Zone" mit starker Verdampfung vorhanden ist, auf die eine entfernte Zone folgt, in der der effektive Verdampfungsanteil auf weniger als 10% der gesamten zugeführten Wärme absinkt. Während die bei diesen Stabbündelversuchen gemessenen Wand- und Dampfübertemperaturen gegenüber früher in Einzelrohrversuchen ermittelten Werten um eine Größenordnung abweichen, wird eine qualitative Übereinstimmung im axialen Verhalten des Filmsiede-Vorgangs beobachtet. Diese Daten werden in der Hoffnung vorgestellt, Anstrengungen zu unterstützen, die zur Entwicklung von verbesserten mechanistischen Modellen für den Wärmeübergang beim Filmsieden in Zwangskonvektion unternommen werden.

КОНВЕКТИВНОЕ ПЛЕНОЧНОЕ КИПЕНИЕ В ПУЧКЕ СТЕРЖНЕЙ: ИЗМЕНЕНИЕ АКСИАЛЬНОЙ СКОРОСТИ ИСПАРЕНИЯ

Аннотация—Экспериментально исследовалось конвективное пленочное кипение (закритический тепловой поток) при двухфазном (пар–вода) обтекании экспериментального пучка из 9 стержней. Измерены значения теплового потока на стенке, перегрева стенки и перегрева пара в зависимости от расстояния по оси от места возникновения критического теплового потока при изменении расхода и паросодержания. Полученные данные позволяют оценить эффективный коэффициент испарения (часть полного потока подводимого тепла, расходуемая на парообразование) как функцию экспериментальных условий и расстояния по оси от точки критического потока. По результатам выявлено существование "ближней области" с интенсивным испарением, за которой следует дальняя область, где эффективный коэффициент испарения снижается и составляет менее 10% полного потока подводимого тепла. Несмотря на то, что значения перегревов стенки и пара, измеренные в исследуемом пучке стержней, отличаются по величине от ранее полученных экспериментальных данных для единичной трубы, наблюдается качественное совпадение результатов для закритического теплового потока в осевом направлении. Результаты работы могут способствовать усовершенствованию моделей конвективного теплообмена при пленочном кипении.